Materials Today Physics 38 (2023) 101240

Contents lists available at ScienceDirect

Materials Today Physics

journal homepage: www.journals.elsevier.com/materials-today-physics

Composite design of half-Heusler thermoelectrics: Selective doping of grain boundary phases in NbFeSb by InSb

Ruben Bueno Villoro [a,*], Raana Hatami Naderloo [b,1], Dominique Alexander Mattlat [a], Chanwon Jung [a], Kornelius Nielsch [b], Christina Scheu [a], Ran He [b,**], Siyuan Zhang [a,***]

[a] Max-Planck-Institut für Eisenforschung GmbH, Max-Planck-Straße 1, 40237, Düsseldorf, Germany
[b] IFW Dresden, Helmholtzstraße 20, 01069, Dresden, Germany

ARTICLE INFO

Keywords:
Thermoelectric materials
Grain boundary engineering
Half Heusler materials
Transmission electron microscopy

ABSTRACT

Thermoelectric materials require complex microstructures to optimize the power conversion efficiency. Grain boundaries (GBs) reduce the thermal conductivity in nanocrystalline materials but often also reduce the electrical conductivity. We have recently shown that elemental segregation at GBs can make them electrically conductive or non-resistive and thereby improving the thermoelectric properties. Nevertheless, the doping elements participate in the chemistry within the grain matrix, which can limit the design space. In this work, we present an independent control of doping to the GBs. Specifically, we add InSb to $Nb_{0.95}Ti_{0.05}FeSb$ to selectively modify the chemistry of the GBs without increasing the carrier concentration of the matrix. Using high resolution transmission electron microscopy and atom probe tomography, we understand the role of InSb in the selective modification of the chemistry of the GBs and we establish structure-property relationships between the chemistry of the GBs and their electrical behaviour. Incorporating InSb into the GBs successfully increases power factor and $zT$of fine-grained $Nb_{0.95}Ti_{0.05}FeSb$. We demonstrate that the negative impact of GBs in the power factor can be overcome by GB engineering.

1. Introduction

Thermoelectric modules are robust solid-state electricity generators suitable for small and distributed power generation and waste heat recovery [1]. Within the modules, thermoelectric materials harvest electricity from gradients of temperature. The performance of thermoelectric materials is evaluated using the dimensionless figure of merit (zT), $zT = \sigma S^2 T/\kappa$, where σ is the electrical conductivity, S the Seebeck coefficient, T the temperature and κ the thermal conductivity. zT enhancement is complex due to the highly interlaced transport of electrons and phonons and the dependence on the microstructure [1].

The thermal conductivity can be reduced by introducing microstructural features such as dislocations [2], stacking faults [3], grain boundaries (GBs) [4–6], and employing crystal structures with complex unit cells [7–9] or rattling atoms [10,11], which can enhance phonon scattering [12]. In bulk thermoelectrics, one of the most discussed concepts is grain size reduction. This can be achieved through the rapid sintering of nanograin or amorphous powders [13] using bottom-up [14,15] or top-down [16] synthesis routes.

Phonons have larger mean free paths than electrons and wider dispersion, and hence it is expected that phonons will be more effectively scattered by GBs [17,18]. Nanostructuring has been successfully applied to materials such as Bi_2Te_3 [19,20], BiCuSeO [21], SiGe [22,23] and half-Heusler materials such as TiCoSb [24] and NbFeSb [25] to achieve a significant reduction in thermal conductivity while maintaining good electrical mobility and power factor. Half-Heusler thermoelectric materials present excellent properties at mid-to-high temperatures, as well as thermal and mechanical robustness [26]. Additionally, the elemental components of these compounds are both earth-abundant and benign [26]. Among the half-Heusler alloys, (Nb,V,Ta)FeSb compounds exhibit the highest p-type performance due to their very high power factors as a result of d-band convergence in the valence

* Corresponding author.
** Corresponding author.
*** Corresponding author.
E-mail addresses: r.bueno@mpie.de (R. Bueno Villoro), r.he@ifw-dresden.de (R. He), siyuan.zhang@mpie.de (S. Zhang).
[1] Equal contributor.

https://doi.org/10.1016/j.mtphys.2023.101240
Received 18 July 2023; Received in revised form 15 September 2023; Accepted 25 September 2023
Available online 30 September 2023

band edge [27–29]. The thermoelectric properties of Ti-doped NbFeSb are strongly correlated with the GBs [25,30,31]. $Nb_{0.95}Ti_{0.05}FeSb$ presents one of the highest power factors among thermoelectric materials, exceeding 100 μW cm^{-1} K^{-2} at room temperature [30]. However, such high power factors are only achieved in coarse-grained materials, and significant reduction is observed as the grain size drops from 1.3 μm to 0.2 μm [25,32]. On the other hand, $Nb_{0.80}Ti_{0.20}FeSb$ displays completely different behavior, as grain size has little impact on the power factor [25, 30].

We have recently shown that $Nb_{1-x}Ti_xFeSb$ contain GB phases that affect the electrical properties of the material [25]. By increasing the Ti content, Ti segregates to the GBs and transition from a resistive GB phase in $Nb_{0.95}Ti_{0.05}FeSb$ to a non-resistive GB phase in $Nb_{0.80}Ti_{0.20}FeSb$ [25]. Although increased Ti doping significantly enhances the conductivity of the GBs, the high solubility of Ti into NbFeSb increases the carrier concentration of the grain interior. As a result, the Seebeck coefficient (and power factor) of $Nb_{0.80}Ti_{0.20}FeSb$ is significantly lowered. At room temperature, S is reduced from 178 to 88 μV K^{-1} (51% reduction) leading to a lower room temperature zT (33% reduction) when comparing $Nb_{0.95}Ti_{0.05}FeSb$ and $Nb_{0.80}Ti_{0.20}FeSb$ [25].

In order to reduce the GB resistivity of NbFeSb without reducing the Seebeck coefficient, the doping concentration should not be modified. This can be achieved by introducing a second dopant that has limited solubility within the NbFeSb grain and thus, segregates to the GBs without increasing the carrier concentration of the grain interior. InSb has been introduced in half-Heusler thermoelectrics such as n-type (Ti, Zr,Hf)(Co,Ni)Sb [33] and p-type Ti(Co,Fe)Sb [34] to successfully enhance their power factor and zT. InSb is a promising thermoelectric material with high carrier mobility and n-type $In_{0.86}Ga_{0.2}Sb$ shows a peak zT of 0.9 at 770 K [35]. In this work, we introduce InSb into $Nb_{0.95}Ti_{0.05}FeSb$ to selectively modify the chemistry at the GBs. We demonstrate that InSb segregates to GBs to suppress the GB resistivity, but does not contribute to doping in the $Nb_{0.95}Ti_{0.05}FeSb$ matrix. As a result, the carrier concentration of the materials is maintained and hence the high Seebeck coefficient. This work provides a path to optimize thermoelectric materials by selective doping at GBs.

2. Results and discussion

2.1. Properties

Elements that present no solubility in NbFeSb are required to modify the GB chemistry without modifying the carrier concentration. In this work, InSb is introduced in $Nb_{0.95}Ti_{0.05}FeSb$ samples to lower the GB resistivity while keeping a high Seebeck coefficient, thus, enhancing the power factor. Since GBs reduce the power factor mainly at low temperature, we have focused our study at temperatures between 300 K and 673 K. Optimization of low temperature zT helps to increase the $zT_{average}$ and is attractive for applications such as thermoelectric cooling [36].

To study the effect of InSb doping, $Nb_{0.95}Ti_{0.05}FeSb$ and $(Nb_{0.95}Ti_{0.05}FeSb)(InSb)_x$ (x = 0.01, 0.02, 0.03) samples were synthesized. As revealed in the x-ray diffraction (XRD) patterns (Fig. 1), NbFeSb half Heusler is the dominant phase in all samples. In the $(Nb_{0.95}Ti_{0.05}FeSb)(InSb)_x$ samples, one small peak of InSb is visible at $2\theta = 46°$. The lattice parameters are 0.594(6) nm for $Nb_{0.95}Ti_{0.05}FeSb$ and 0.594(5) nm, 0.594(4) nm and 0.594(5) nm for $(Nb_{0.95}Ti_{0.05}FeSb)(InSb)_{0.01}$, $(Nb_{0.95}Ti_{0.05}FeSb)(InSb)_{0.02}$ and $(Nb_{0.95}Ti_{0.05}FeSb)(InSb)_{0.03}$ respectively. Thus, they are in good agreement with literature and the differences between samples are negligible [25,37].

The addition of InSb has a positive effect on the power factor (PF). The PF of $Nb_{0.95}Ti_{0.05}FeSb$ samples with no InSb (blue), 1% (orange), 2% (purple) and 3% (red) InSb are presented in Fig. 2a. $(Nb_{0.95}Ti_{0.05}FeSb)(InSb)_{0.02}$ presents the highest increase on PF (116% increase at room temperature respect to the sample with no InSb), and is thus, selected as the optimized sample for a detailed study. The impact of InSb in the power factor is due to the increase in the electrical conductivity

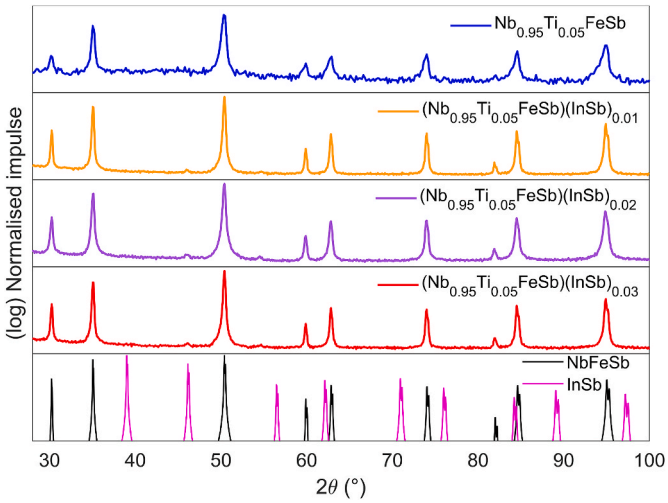

Fig. 1. XRD patterns of $Nb_{0.95}Ti_{0.05}FeSb$ (blue) and $(Nb_{0.95}Ti_{0.05}FeSb)(InSb)_{0.01}$ (orange), $(Nb_{0.95}Ti_{0.05}FeSb)(InSb)_{0.02}$ (purple) and $(Nb_{0.95}Ti_{0.05}FeSb)(InSb)_{0.03}$ (red). The calculated references of NbFeSb (black) and InSb (magenta) are plotted for comparison.

(120% increase at room temperature) (Fig. 2b) while Seebeck coefficient is only reduced by 1% (Fig. 2c).

Hall carrier concentration is measured for $Nb_{0.95}Ti_{0.05}FeSb$ and $(Nb_{0.95}Ti_{0.05}FeSb)(InSb)_{0.02}$ being 9.9×10^{20} cm^{-3} and 1.1×10^{21} cm^{-3} respectively. Thus, a negligible difference in carrier concentration is observed. This suggests that InSb has not been incorporated into the NbFeSb lattice (carrier concentration and Seebeck coefficient unaffected) but it has clearly enhanced the electrical conductivity. Such change can be explained by a transition from resistive to non-resistive GBs due to changes in the chemistry of the GBs [25].The stability over time and upon cycling of $(Nb_{0.95}Ti_{0.05}FeSb)(InSb)_{0.02}$ is studied. $(Nb_{0.95}Ti_{0.05}FeSb)(InSb)_{0.02}$ samples are cycled 5 times up to 973 K. Minimal differences in the electrical conductivity (Supplemental Fig. 1a) and Seebeck coefficient (Supplemental Fig. 1b) are observed, thus, we conclude that the samples are stable upon cycling. The $(Nb_{0.95}Ti_{0.05}FeSb)(InSb)_{0.02}$ sample used within this work has been remeasured after 2 years exposed in air presenting little changes (6% and <1% difference in electrical conductivity and Seebeck coefficient respectively at room temperature), thus, the sample is stable over time and exposed to air. Those results are presented in Supplemental Fig. 2.

As the electrical properties of $Nb_{0.95}Ti_{0.05}FeSb$ are known to be sensitive to the grain size, we take special care to compare samples with similar grain sizes. As shown in Fig. 3, we have achieved samples with average grain sizes of 350 nm and 340 nm for $Nb_{0.95}Ti_{0.05}FeSb$ and $(Nb_{0.95}Ti_{0.05}FeSb)(InSb)_{0.02}$. For the same grain size, the addition of InSb in $Nb_{0.95}Ti_{0.05}FeSb$ increases the electrical conductivity (Fig. 2b). As the Seebeck coefficient (Fig. 2c) of $(Nb_{0.95}Ti_{0.05}FeSb)(InSb)_{0.02}$ is maintained, the increase in the power factor is proportional to the increase in the electrical conductivity (Fig. 3).

In contrast, the previous strategy to increase electrical conductivity by Ti doping achieved similar increase in the electrical conductivity, but at the expense of decreasing Seebeck coefficient [25]. This is because Ti has a high solubility in NbFeSb and increases the carrier concentration in the matrix. As a result, the Seebeck coefficient of $Nb_{0.80}Ti_{0.20}FeSb$ is reduced (Fig. 4a), and the power factor only has marginal improvement at room temperature with respect to $Nb_{095}Ti_{0.05}FeSb$ (Fig. 3b). This is a common constraint for thermoelectric design, as for each temperature, there is only one optimal carrier concentration to maximize the power factor [38,39]. This comparison shows the positive impact of adding InSb and suggests that the GB resistivity can be suppressed without the need of changing the chemistry (and the carrier concentration) of the matrix.

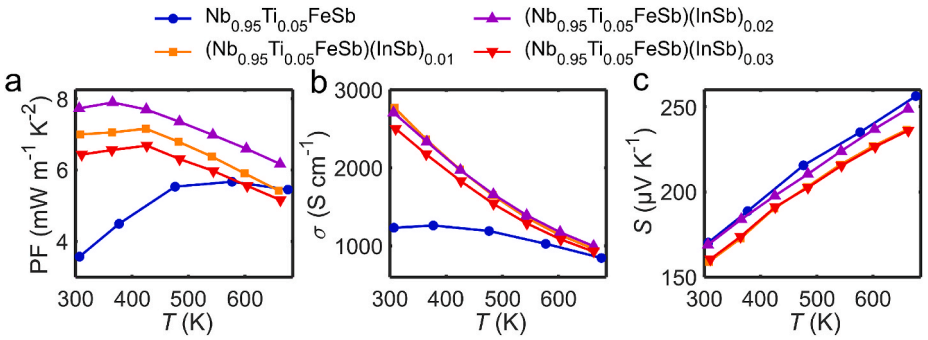

Fig. 2. InSb increases the (a) power factor (PF) by increasing the (b) electrical conductivity of $Nb_{0.95}Ti_{0.05}FeSb$ samples with 1% InSb (orange), 2% InSb (purple) and 3% InSb (red) compared to samples without InSb (blue) without significantly decreasing (c) the Seebeck coefficient. $(Nb_{0.95}Ti_{0.05}FeSb)(InSb)_{0.02}$ is selected as the optimal sample since it maximizes the power factor.

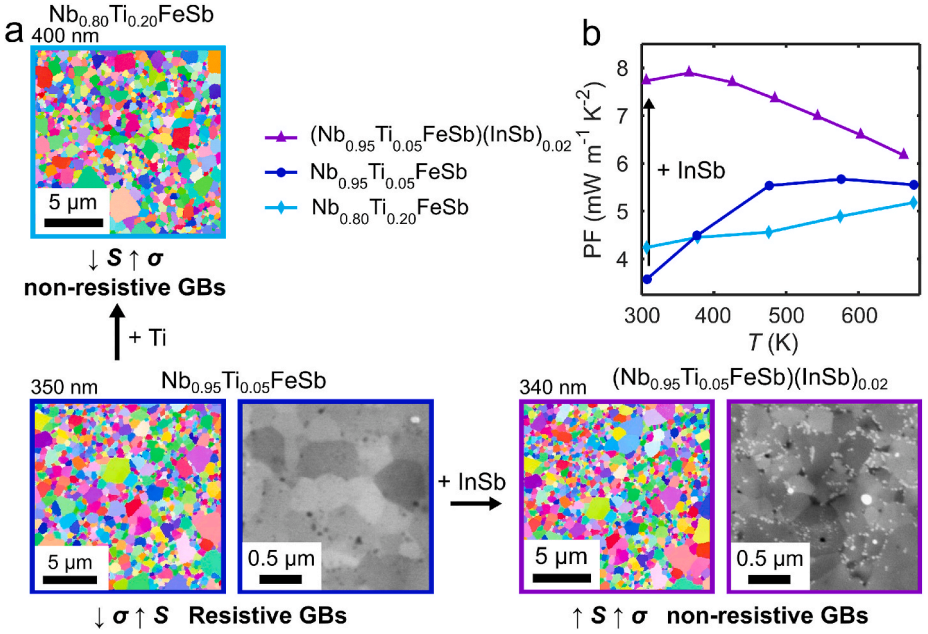

Fig. 3. (a) EBSD maps of $Nb_{0.95}Ti_{0.05}FeSb$ (blue), $(Nb_{0.95}Ti_{0.05}FeSb)(InSb)_{0.02}$ (purple) and $Nb_{0.80}Ti_{0.20}FeSb$ (cyan) show that grain size is almost identical in all samples. SEM images of $(Nb_{0.95}Ti_{0.05}FeSb)(InSb)_{0.02}$ contain small particles around the GBs that are not present in $Nb_{0.95}Ti_{0.05}FeSb$. (b) The power factor vs T plot shows that $(Nb_{0.95}Ti_{0.05}FeSb)(InSb)_{0.02}$ has a higher power factor than $Nb_{0.95}Ti_{0.05}FeSb$ (due to an increased electrical conductivity) and $Nb_{0.80}Ti_{0.20}FeSb$ (due to increased Seebeck coefficient). $Nb_{0.80}Ti_{0.20}FeSb$ data is taken from Ref. [25].

The SEM image of $(Nb_{0.95}Ti_{0.05}FeSb)(InSb)_{0.02}$ reveals the presence of bright particles at the GBs that are not present on the SEM image of $Nb_{0.95}Ti_{0.05}FeSb$ suggesting that InSb particles are accumulated at the GBs. A more detailed TEM analysis is given below.

At similar grain size, 10% reduction of thermal conductivity at room temperature is observed by adding 2%InSb to $Nb_{0.95}Ti_{0.05}FeSb$ (Fig. 4b). This is attributed to enhanced phonon scattering by the densely distributed In-rich particles at the GBs(Fig. 3b). In comparison, higher amount of Ti doping in $Nb_{0.80}Ti_{0.20}FeSb$ causes even more reduction in the thermal conductivity due to enhanced phonon scattering by Ti solute substitution in the matrix [25]. Overall, as shown in Fig. 4c, In-doping leads to the highest zT at temperatures below 650 K. At higher temperature, the optimal carrier concentration is higher [30,32], so that the more heavily p-doped $Nb_{0.80}Ti_{0.20}FeSb$ outperforms samples with base concentrations of $Nb_{0.95}Ti_{0.05}FeSb$ with or without In doping.

2.2. Chemistry

Scanning transmission electron microscopy (STEM) coupled with energy dispersive x-ray spectroscopy (EDX) and atom probe tomography (APT) are performed to determine the impact of InSb in the microstructure and properties. The 3D atom map (Fig. 5a) shows that the GBs are enriched in In (In atoms are highlighted). The 1D concentration profile (Fig. 5b) shows that the GB is enriched in In and Sb and is poor in Nb. The magnified concentration profile of In (Fig. 5c) reveals that the max. In content is ~ 0.8 at.% corresponding to a Gibbsian excess of 1.7 ± 0.3 atoms nm^{-2}. In previous studies in $Nb_{1-x}Ti_xFeSb$, we reported that Fe-rich GBs present a resistive behaviour while Ti-rich GBs present a non-resistive behaviour [25]. The GBs of $(Nb_{0.95}Ti_{0.05}FeSb)(InSb)_{0.02}$) are Fe-poor but instead of Ti-rich, they are In-rich. Thus, the addition of In modifies the chemistry of the GBs and they become non-resistive without the need of additional Ti. The content of In in the matrix is measured in the area contained in the black rectangle of Fig. 5a (80 nm^3). Of 2106982 atoms, 321 were detected as In, which corresponds to an In concentration of 0.015 at.% and is above the detection limit of the technique (detection limit ~ 0.004 at.%).These results confirm that In has a negligible solubility in NbFeSb and that the GBs are enriched in In. As such, In modifies the chemistry of the GBs without modifying the chemistry of the matrix.

In- and Sb-rich particles (purple squares) are observed with STEM-

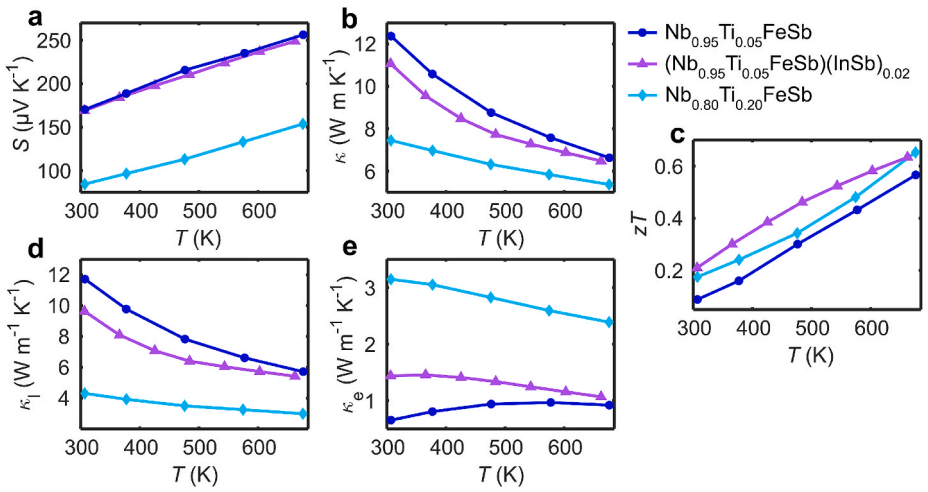

Fig. 4. (a) Seebeck coefficient (S), (b) thermal conductivity (κ), (c) zT factor, (d) lattice thermal conductivity (κ_l) and (e) electronic thermal conductivity (κ_e) for $Nb_{0.95}Ti_{0.05}FeSb$ (blue), $Nb_{0.80}Ti_{0.20}FeSb$ (cyan) and $(Nb_{0.95}Ti_{0.05}FeSb)(InSb)_{0.02}$ (purple).

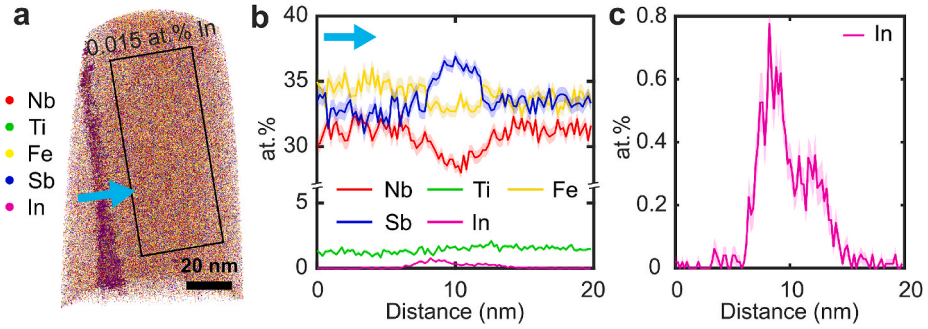

Fig. 5. (a)APT 3D atom map of $(Nb_{0.95}Ti_{0.05}FeSb)(InSb)_{0.02}$ (In atoms highlighted), (b) 1D concentration profile across a GB (light blue line) presenting In and Sb enrichment and Nb depletion. (c) 1D concentration profile of In presents clear enrichment at the GB while only ~ 0.015 at.% In is detected at the matrix.

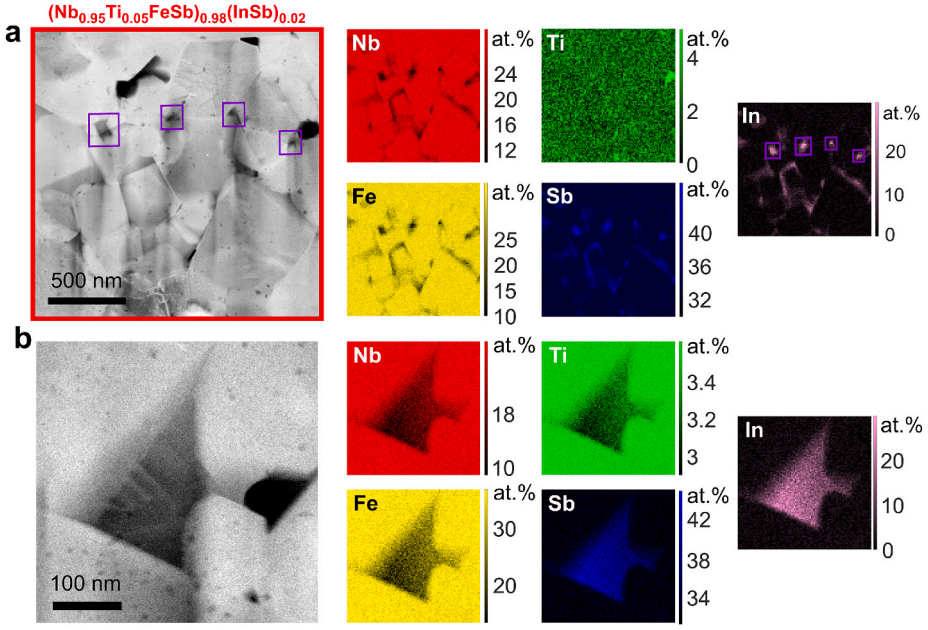

Fig. 6. (a) HAADF-STEM image of a region containing several grains and In-,Sb-rich particles (purple squares) with EDX maps for Nb (red), Ti (green), Fe (yellow), Sb (blue) and In (purple). (b) EDX maps of a In-, Sb-rich particle.

EDX (Fig. 6a). The particles are studied in more detail in Fig. 6b. Their quantification is compatible with 50% InSb +50% $Nb_{0.95}Ti_{0.05}FeSb$. These results confirm that the excess In is accumulated in the form of particles at the GBs, as seen in Fig. 3a, and also extend to the GBs (as seen in Fig. 5).

These results show that In is incorporated selectively at the GBs and reduces the GB resistivity, thus, enhancing the power factor by an 116% and the zT by 137% at room temperature.

In this work, we present a design strategy to optimize the carrier transport in the matrix and the GB phase separately. Firstly, the carrier concentration in the matrix is optimized by an alloy dopant (in this case, Ti) to reach the optimal power factor. Then, the GB dopant (in this case, In) is added to lower the electrical resistivity through the GB. In a previous work [25], we have shown that in NbFeSb half-Heusler, heavy Ti doping (20%) can serve to optimize the matrix and GB transport simultaneously. However, at lower temperature, the optimal Ti doping for the matrix is much lower (5%) and unable to sustain a conductive GB. In this case, we showed that In can be introduced as a GB dopant to significantly enhance the GB conductivity.

Such design strategy can be widely applied in fine-grained thermoelectric materials. The matrix dopant needs to be optimized first, and then the GB dopant has to be carefully chosen. Firstly, it should be a conductive phase like InSb to enhance the GB conductivity. Secondly, it should have minimal solubility into the matrix phase, or otherwise the optimal doping level in the matrix would be exceeded. InSb has been proven a great candidate for NbFeSb (this work), (Ti,Zr,Hf)(Co,Ni)Sb [33] and Ti(Co,Fe)Sb [34]. The search for efficient GB dopants for other compounds would extend the design principle to more classes of semiconductor materials and devices.

3. Conclusion

In this work, the chemistry of the GBs of $Nb_{0.95}Ti_{0.05}FeSb$ has been selectively modified by introducing InSb. Since In has a negligible solubility in NbFeSb, the carrier concentration and Seebeck coefficient has not been affected by the addition of InSb. Instead, the modification of the GB chemistry reduces the GB resistivity, thereby increasing the power factor and zT between 300 K and 673 K of $(Nb_{0.95}Ti_{0.05}FeSb)(InSb)_{0.02}$ compared to samples without InSb with almost identical grain size. Therefore, this work provides a pathway to optimize the GB chemistry (and zT) without modifying the chemistry of the grain interior.

This work demonstrates that the chemistry of the GBs can be selectively tuned to reduce the GB resistivity without modifying the doping level of the matrix. This approach enables the use of GB engineering to optimize the properties of thermoelectric materials by carefully selecting GB dopants that have no solubility in the matrix.

4. Experimental section

4.1. Synthesis

$Nb_{0.95}Ti_{0.05}FeSb$ and $(Nb_{0.95}Ti_{0.05}FeSb)(InSb)x$ (x = 0.01, 0.02, 0.03) half-Heusler samples were prepared by a two-step ball-milling and hot-pressing method. For the ball-milling process, 10 g of raw elements, including Nb powders (99.8%, Alfa Aesar), Fe granules (99.98%, Alfa Aesar), Ti sponges (99.95%, Alfa Aesar), In shot (99.9%, Alfa Aesar) and Sb pieces (99.999%, MaTecK) were weighted stoichiometrically and loaded into stain steel jars in a glove-box (argon atmosphere) and ball milled for 12 h to produce nano-powder. Afterwards the ball milling powders were compacted to a disk by a direct current induced hot-pressing under a pressure of 50 MPa in vacuum for 3 min at 1123 K samples with InSb. The densities of the sintered sample are 99% of theoretical densities.

4.2. Property measurement

The sintered compounds were cut and polished to the desired sizes for measuring the transport properties. The Seebeck coefficient (S) and electrical conductivity (σ) were obtained by using a commercial device LSR-3 (Linseis) system at the same time. The thermal conductivity (κ) was calculated as a multiplication of thermal diffusivity (D) (LFA-Linseis), specific heat (C_p), and mass density (d) (Archimedes' kit) ($\kappa = DC_pd$). The measurement errors were 4%, 5%, and 12% for σ, S, and κ, respectively. The uncertainties of κ originated from 2% in mass density, 4% in diffusivity, and 6% in specific heat. Therefore, the uncertainties in power factor and zT were 10% and 20%, respectively. To increase the readability of the graphs, the error bars were not added on the curves. Hall carrier concentration (n), was measured via a commercial system (PPMS DaynaCool, Quantum Design with a magnetic field of ±9 T and an electric current of 8 mA). Lorenz factor is calculated as described in Kim et al. [40].

4.3. Microstructure characterization

Solid XRD was performed on polished surfaces using a Rigaku Smartlab 9 KW difractometer with a Cu K_α source ($\lambda = 0.154059$ nm). The lattice parameters were obtained using the Bragg's law on the 10 main peaks of the XRD and the reference peaks were calculated using Vesta [41] with the experimental lattice parameters.

Samples were prepared for SEM investigation using SiC papers for grinding and diamond and OPS suspension solutions for polishing. SEM characterization was performed in a Sigma 500 Zeiss microscope operated at 15 kV. EBSD was acquired at 15 kV, 10 nA and a working distance of 20 mm using a EDAX/TSL system with a Hikari camera.

A Scios2 Thermo Fisher focused ion beam (FIB) was used to prepare specimens for STEM and APT investigations using a general procedure described by Schaffer et al. [42] and Thompson et al. [43] respectively. STEM specimens were thinned to < 150 nm by 30 kV Ga^+ beam, and final thinning and cleaning were performed at 5 and 2 kV.

STEM experiments were performed in a Thermo Fisher Titan Themis probe-corrected microscope operated at 300 kV with a collection semiangle of 24 mrad and ~ 0.1 nm probe size. HAADF-STEM images were acquired using a collection angle of 73–200 mrad and a pixel dwell time of 1–2 μs. STEM-EDX maps were acquired using a four-quadrant silicon-drift EDX detector (Super-X) in ~ 30 min acquisition time for each map. Multivariate statistical analysis was performed for noise reduction [44] and the Cliff–Lorimer formula was used for elemental quantification.

APT experiments were performed using a local electrode atom probe (CAMECA LEAP 5000 XR) in pulsed laser mode at a specimen base temperature of ~ 60 K and detection rate of 1%. The laser pulse energy and frequency were set to 30 pJ and 125 kHz, respectively. Data reconstruction and analyses were done with AP suite 6.1 software, provided by CAMECA Instruments.

CRediT authorship contribution statement

Ruben Bueno Villoro: Conceptualization, Formal analysis, Data curation, Investigation, Writing – original draft, Writing – review & editing. **Raana Hatami Naderloo:** Conceptualization, Investigation, Writing – review & editing. **Dominique Alexander Mattlat:** Investigation. **Chanwon Jung:** Investigation, Writing – review & editing. **Kornelius Nielsch:** Writing – review & editing. **Christina Scheu:** Writing – review & editing. **Ran He:** Conceptualization, Writing – review & editing, Supervision. **Siyuan Zhang:** Conceptualization, Writing – review & editing, Supervision.

Declaration of competing interest

The authors declare that they have no known competing financial interests or personal relationships that could have appeared to influence

the work reported in this paper.

Data availability

Data will be made available on request.

Acknowledgements

R.B.V. acknowledges the support from the International Max Planck Research School for Interface Controlled Materials for Energy Conversion (IMPRS-SurMat). C.J. acknowledges the support from the Basic Science Research Program of the National Research Foundation of Korea (NRF) (grant number 2021R1A6A3A03045488) C.S. acknowledges funding from the German research foundation (DFG) within the Collaborative Research Centre SFB 1394 "Structural and Chemical Atomic Complexity — From Defect Phase Diagrams to Materials Properties" (Project ID 409476157). R.H. acknowledges financial support from the DFG, Project Number 453261231. S.Z. acknowledges funding from the DFG under the framework of SPP 2370 (Project number: 502202153).

Appendix A. Supplementary data

Supplementary data to this article can be found online at https://doi.org/10.1016/j.mtphys.2023.101240.

References

[1] G.J. Snyder, E.S. Toberer, Nat. Mater. 7 (2008) 2–105.
[2] L. Abdellaoui, Z. Chen, Y. Yu, T. Luo, R. Hanus, T. Schwarz, R. Bueno Villoro, O. Cojocaru-Mirédin, G.J. Snyder, D. Raabe, Y. Pei, C. Scheu, S. Zhang, Adv. Funct. Mater. 31 (20) (2021) 2101214.
[3] L. Abdellaoui, S. Zhang, S. Zaefferer, R. Bueno-Villoro, A. Baranovskiy, O. Cojocaru-Mirédin, Y. Yu, Y. Amouyal, D. Raabe, G.J. Snyder, C. Scheu, Acta Mater. 178 (2019) 135.
[4] A. Sood, R. Cheaito, T. Bai, H. Kwon, Y. Wang, C. Li, L. Yates, T. Bougher, S. Graham, M. Asheghi, M. Goorsky, K.E. Goodson, Nano Lett. 18 (6) (2018) 3466.
[5] H. Dong, B. Wen, R. Melnik, Sci. Rep. 4 (1) (2014) 7037.
[6] P.G. Klemens, Int. J. Thermophys. 15 (6) (1994) 1345.
[7] A. Zevalkink, Y. Takagiwa, K. Kitahara, K. Kimura, G.J. Snyder, Dalton Trans. 43 (12) (2014) 4720.
[8] S. Lin, W. Li, Y. Pei, Mater. Today 48 (2021) 198.
[9] E.S. Landry, M.I. Hussein, A.J.H. McGaughey, Phys. Rev. B 77 (18) (2008) 184302.
[10] B.C. Sales, D. Mandrus, R.K. Williams, Science 272 (1996) 5266, 1325.
[11] G.S. Nolas, J.L. Cohn, G.A. Slack, S.B. Schujman, Appl. Phys. Lett. 73 (2) (1998) 178.
[12] P.G. Klemens, in: F. Seitz, D. Turnbull (Eds.), Solid State Physics, 7, Academic Press, 1958, pp. 1–98, 0081-1947.
[13] C. Jung, K. Jang, H. Park, J. Jang, H. Jang, B. Kang, K. Park, S. Zhang, R.B. Villoro, S. Park, H.J. Ryu, Y.S. Jung, M.-W. Oh, C. Scheu, S.-H. Yi, P.-P. Choi, J. Mater. Sci. Technol. 165 (2023) 39.
[14] X.B. Zhao, X.H. Ji, Y.H. Zhang, T.J. Zhu, J.P. Tu, X.B. Zhang, Appl. Phys. Lett. 86 (2005) 6 62111.
[15] N. Nandihalli, D.H. Gregory, T. Mori, Adv. Sci. 9 (25) (2022) 2106052.
[16] G. Rogl, A. Grytsiv, K. Yubuta, S. Puchegger, E. Bauer, C. Raju, R.C. Mallik, P. Rogl, Acta Mater. 95 (2015) 201.
[17] M. Zebarjadi, K. Esfarjani, M.S. Dresselhaus, Z.F. Ren, G. Chen, Energy Environ. Sci. 5 (1) (2012) 5147.
[18] J. Zhou, H. Zhu, T.-H. Liu, Q. Song, R. He, J. Mao, Z. Liu, W. Ren, B. Liao, D. J. Singh, Z. Ren, G. Chen, Nat. Commun. 9 (1) (2018) 1721.
[19] B. Poudel, Q. Hao, Y. Ma, Y. Lan, A. Minnich, B. Yu, X. Yan, D. Wang, A. Muto, D. Vashaee, X. Chen, J. Liu, M.S. Dresselhaus, G. Chen, Z. Ren, Science 320 (5876) (2008) 634.
[20] S. Sumithra, N.J. Takas, D.K. Misra, W.M. Nolting, P.F.P. Poudeu, K.L. Stokes, Adv. Energy Mater. 1 (6) (2011) 1141.
[21] J. Li, J. Sui, Y. Pei, C. Barreteau, D. Berardan, N. Dragoe, W. Cai, J. He, L.-D. Zhao, Energy Environ. Sci. 5 (9) (2012) 8543.
[22] G. Joshi, H. Lee, Y. Lan, X. Wang, G. Zhu, D. Wang, R.W. Gould, D.C. Cuff, M. Y. Tang, M.S. Dresselhaus, G. Chen, Z. Ren, Nano Lett. 8 (12) (2008) 4670.
[23] X.W. Wang, H. Lee, Y.C. Lan, G.H. Zhu, G. Joshi, D.Z. Wang, J. Yang, A.J. Muto, M. Y. Tang, J. Klatsky, S. Song, M.S. Dresselhaus, G. Chen, Z.F. Ren, Appl. Phys. Lett. 93 (19) (2008) 193121.
[24] R. Bueno Villoro, M. Wood, T. Luo, H. Bishara, L. Abdellaoui, D. Zavanelli, B. Gault, G.J. Snyder, C. Scheu, S. Zhang, Acta Mater. (2023) 118816.
[25] R. Bueno Villoro, D. Zavanelli, C. Jung, D.A. Mattlat, R. Hatami Naderloo, N. Pérez, K. Nielsch, G.J. Snyder, C. Scheu, R. He, S. Zhang, Adv. Energy Mater. (2023) 2204321.
[26] R.J. Quinn, J.-W.G. Bos, Mater. Adv. 2 (19) (2021) 6246.
[27] C. Fu, T. Zhu, Y. Pei, H. Xie, H. Wang, G.J. Snyder, Y. Liu, Y. Liu, X. Zhao, Adv. Energy Mater. 4 (18) (2014) 1400600.
[28] M.K. Brod, S. Anand, G.J. Snyder, Adv. Electron. Mater. 8 (4) (2022) 2101367.
[29] M.K. Brod, S. Guo, Y. Zhang, G.J. Snyder, MRS Bull. 47 (2022) 6–573.
[30] R. He, D. Kraemer, J. Mao, L. Zeng, Q. Jie, Y. Lan, C. Li, J. Shuai, H.S. Kim, Y. Liu, D. Broido, C.-W.W. Chu, G. Chen, Z. Ren, Proc. Natl. Acad. Sci. USA 113 (48) (2016) 13576. LP).
[31] Q. Qiu, Y. Liu, K. Xia, T. Fang, J. Yu, X. Zhao, T. Zhu, Adv. Energy Mater. 9 (11) (2019) 1803447.
[32] C. Hu, K. Xia, C. Fu, X. Zhao, T. Zhu, Energy Environ. Sci. 15 (4) (2022) 1406.
[33] W.J. Xie, J. He, S. Zhu, X.L. Su, S.Y. Wang, T. Holgate, J.W. Graff, V. Ponnambalam, S.J. Poon, X.F. Tang, Q.J. Zhang, T.M. Tritt, Acta Mater. 58 (14) (2010) 4705.
[34] W.J. Xie, Y.G. Yan, S. Zhu, M. Zhou, S. Populoh, K. Galazka, S.J. Poon, A. Weidenkaff, J. He, X.F. Tang, T.M. Tritt, Acta Mater. 61 (6) (2013) 2087.
[35] Z. Du, M. Yan, J. Zhu, Mater. Res. Express 5 (10) (2018) 106301.
[36] W.-Y. Chen, X.-L. Shi, J. Zou, Z.-G. Chen, Small Methods 6 (2) (2022) 2101235.
[37] C. Fu, T. Zhu, Y. Liu, H. Xie, X. Zhao, Energy Environ. Sci. 8 (1) (2015) 216.
[38] Y. Pei, Z.M. Gibbs, A. Gloskovskii, B. Balke, W.G. Zeier, G.J. Snyder, Adv. Energy Mater. 4 (13) (2014) 1400486.
[39] Y. Yu, C. Zhou, X. Zhang, L. Abdellaoui, C. Doberstein, B. Berkels, B. Ge, G. Qiao, C. Scheu, M. Wuttig, O. Cojocaru-Mirédin, S. Zhang, Nano Energy 101 (2022) 107576.
[40] H.-S. Kim, Z.M. Gibbs, Y. Tang, H. Wang, G.J. Snyder, Apl. Mater. 3 (4) (2015) 41506.
[41] K. Momma, F. Izumi, J. Appl. Crystallogr. 41 (3) (2008) 653.
[42] M. Schaffer, B. Schaffer, Q. Ramasse, Ultramicroscopy 114 (2012) 62.
[43] K. Thompson, D. Lawrence, D.J. Larson, J.D. Olson, T.F. Kelly, B. Gorman, Ultramicroscopy 107 (2007) 2–131.
[44] S. Zhang, C. Scheu, Microscopy 67 (2018) suppl_1 i133.